Engineering Fracture Mechanics 264 (2022) 108330

Contents lists available at ScienceDirect

Engineering Fracture Mechanics

journal homepage: www.elsevier.com/locate/engfracmech

Humidity dependence of fracture toughness of cellulose fibrous networks

Russell Spiewak [a,1], Gnana Saurya Vankayalapati [a,1], John M. Considine [b], Kevin T. Turner [a], Prashant K. Purohit [a,*]

[a] Department of Mechanical Engineering and Applied Mechanics, University of Pennsylvania, Philadelphia, PA 19104, USA
[b] USDA Forest Products Laboratory, Madison, WI 53726, USA

ARTICLE INFO

Keywords:
Cohesive law
Fracture toughness
Double cantilever beam
Moisture content

ABSTRACT

Cellulose-based materials are increasingly finding applications in technology due to their sustainability and biodegradability. The sensitivity of cellulose fiber networks to environmental conditions such as temperature and humidity is well known. Yet, there is an incomplete understanding of the dependence of the fracture toughness of cellulose networks on environmental conditions. In the current study, we assess the effect of moisture content on the out-of-plane (i.e., z-dir.) fracture toughness of a particular cellulose network, specifically Whatman cellulose filter paper. Experimental measurements are performed at 16% RH along the desorption isotherm and 23, 37, 50, 75% RH along the adsorption isotherm using out-of-plane tensile tests and double cantilever beam (DCB) tests. Cohesive zone modeling and finite element simulations are used to extract quantitative properties that describe the crack growth behavior. Overall, the fracture toughness of filter paper decreased with increasing humidity. Additionally, a novel model is developed to capture the high peak and sudden drop in the experimental force measurement caused by the existence of an initiation region. This model is found to be in good agreement with experimental data. The relative effect of each independent cohesive parameter is explored to better understand the cohesive zone-based humidity dependence model. The methods described here may be applied to study rupture of other fiber networks with weak bonds.

1. Introduction

Cellulose is an abundantly available polymer in nature. Cellulose networks have good mechanical [1,2] and barrier [3] properties. Filter paper is a network consisting of pure cellulose fibers bound to each other mechanically by entanglement and chemically by hydrogen bonds. The cellulose fibers are flattened hollow tubes, typically 25–35 micrometers wide with thicknesses of 1 to 4 micrometers. When the paper is loaded in tension, permanent deformation occurs through the breaking of inter-fiber bonds (namely, a surface area of multiple hydrogen bonds connecting two fibers) [4,5] and removal of microcrimps. These cellulose networks can fail when subjected to tensile loads during manufacture or in successive operations. It has been demonstrated [6] that these failures generally occur due to rapid propagation of cracks from pre-existing flaws, such as notches or creases. On account of the presence of a stress concentration around a flaw, the stress at which failure occurs is well below the strength of an un-flawed sheet, thus making fracture toughness, the ability of cellulose networks to resist crack growth, an important performance parameter to be studied.

* Corresponding author.
E-mail addresses: kturner@seas.upenn.edu (K.T. Turner), purohit@seas.upenn.edu (P.K. Purohit).
[1] Co-first authors.

https://doi.org/10.1016/j.engfracmech.2022.108330
Received 4 November 2021; Received in revised form 11 February 2022; Accepted 12 February 2022
Available online 23 February 2022
0013-7944/

Previous work in the application of fracture mechanics to paper has been carried out by Wanigaratne [7], Tryding et al. [8] and Zechner et al. [9]. Work of fracture methods that were developed to estimate the fracture toughness of ductile materials have been applied to paper [10,11]. Atomistic modeling of cellulose networks has also been used to shed light on the fracture of paper [12]. There are some works using cohesive zone modeling to model the fracture of paper, including [9,13–15]. Zechner et al. [9] developed a method combining images from experiments with cohesive zone modeling to reliably determine the crack tip, and therefore also the fracture initiation toughness value, of commercial printing paper. Mao et al. [13] used a cohesive zone model to describe the fracture behavior of notched cellulose nanopaper, commercial printing paper, and buckypaper. Makela and Ostlund [14] studied fracture of copy paper along combinations of machine- and cross-directions, also utilizing a cohesive zone model. Meng et al. [15] modeled fracture of cellulose nanofibril network papers using cohesive zone properties derived from the potential energy differences during fiber pullout at the interfaces between hydrogen bonds at a molecular scale. These previous works have shown that cohesive zone modeling is an effective technique to estimate the fracture toughness of cellulose networks, which otherwise cannot be evaluated accurately as these networks exhibit a nonlinear and ductile fracture behavior, but no work has been done extending this technique to study the influence of humidity on these networks.

The macroscale behavior of fibrous networks, in general, depends on the properties of the fibers and the bonds between the fibers; the effects of microscale fiber properties on macroscale material behavior have been studied in networks of random fibers [16–20] and of fibers with cellular shapes [20–22], using large scale finite element simulations. Since fibrous networks generally perform structural functions, their macroscale mechanical properties such as fracture toughness are of critical importance. Network rupture has been studied in [19] by allowing the bonds connecting the fibers to fail in tension as well as shear through finite element simulations of three-dimensional isotropic random fiber networks. However, while it is true that fibrous materials can be three-dimensionally isotropic, they are also often found as sheets which are orthotropic in nature. It is difficult to identify the z-direction properties of thin web orthotropic materials, so fracture studies of such materials are few. Since cellulose papers are a common two-dimensional fibrous network we use it as a vehicle to develop methods to characterize fracture toughness of such materials.

Additionally, as mentioned previously, rupture has been studied in [19] in generalized three-dimensional random fibrous networks by allowing the bonds connecting the fibers to fail. The resulting stress–stretch curves show an initial positive slope which decreases to zero as more bonds break, then the slope of the stress–stretch curve becomes negative and the stress ultimately goes to zero. This resembles traction-separation laws used in cohesive-zone modeling, which account for damage accumulation. Similar stress–strain curves were obtained by [23], who studied mechanics of random fiber networks using stochastic breaking of bonds.

The properties of paper in the thickness direction (i.e., z-direction), although not necessary for conventional paper use and difficult to measure since the characteristic length scales are of the same order of magnitude as the fibrous microstructure of the material, are needed to extend the use of paper for novel applications such as in the fabrication of piezoelectric cellulose sheets and batteries [24–27], Moreover, the information about the out-of-plane properties of paper are helpful in studying scoring, folding and 3-D forming operations.

Earlier works of measuring the mechanical properties of paper in the z-direction are few [28–31]. Nygards et al. [29] used a double notch shear (DNS) test to measure the out-of-plane shear strength of paperboard. The DNS test is advantageous because of its ability to overcome the potential drawbacks arising from the conventional out-of-plane tests which require the paper to be glued between rigid blocks. Ostlund et al. [28] developed experimental techniques to measure the out-of-plane normal and shear properties of paperboard using an extended double notch shear test.

Humidity is an important parameter that can significantly affect the mechanical properties of cellulose networks. Increases in environmental humidity increases the moisture content in the paper and in turn reduces the stiffness of the fibers and the number of fiber–fiber bonds, and thus lead to mechanical changes of the overall network. The effect of humidity on the mechanical and fracture properties of paper is important during converting operations and use by consumers.

Many studies have examined the effect of humidity on the tensile properties of cellulose networks [32–42]. Gamstedt et al. [32] and Celino et al. [33] reviewed works involving moisture-induced softening and swelling of plant and natural cellulose fiber composites. Placet et al. [35] found that water sorption showed a significant influence on the tensile properties and fracture mode of cellulose-based hemp fibers. Alamri et al. [36] investigated cellulose-reinforced epoxy composites at two different humidities and found that strength, modulus, and fracture toughness decreased as a result of moisture absorption. Benitez et al. [37], and Meng et al. [38] also observed decrease in modulus, strength and tensile toughness of cellulose nanopaper sheets with the increase of relative humidity as a result of easier interfacial debonding between cellulose nanofibers (CNFs), which they attribute to moisture induced bond weakening. Benitez et al. [37] also showed a clear transition of the fracture mechanism of cellulose nanopaper network from brittle to pull-out phenomena when varied between 0 and 100% RH. Moropoulou et al. [39] reported a decrease in the tensile strength of filter paper with increase in moisture content and also showed the hysteresis effect of adsorption and desorption. Nissan et al. [40] explored the effect of moisture on the Young's modulus of hydrogen bond dominated solids like paper, and also established an empirical relation between the modulus and moisture content. Of all the aforementioned earlier works involving both pure cellulose (micro and nano) networks and cellulose-based composites, the effect of humidity on the fracture toughness of porous cellulose networks has not been studied.

The objectives of this work are to characterize the z-direction properties using tensile tests and out-of-plane fracture of filter paper (a porous 100% cellulose network) as a function of moisture content using a double cantilever beam (DCB) specimen and model the fracture properties using cohesive zone modeling. Continuum cohesive zone models provide the convenience of tuning a few parameters such as peak stress and separation at failure to model one-dimensional fracture propagation. Use of cohesive zone models also allows us to bypass expensive finite element simulations of discrete fiber networks which require the specification of a

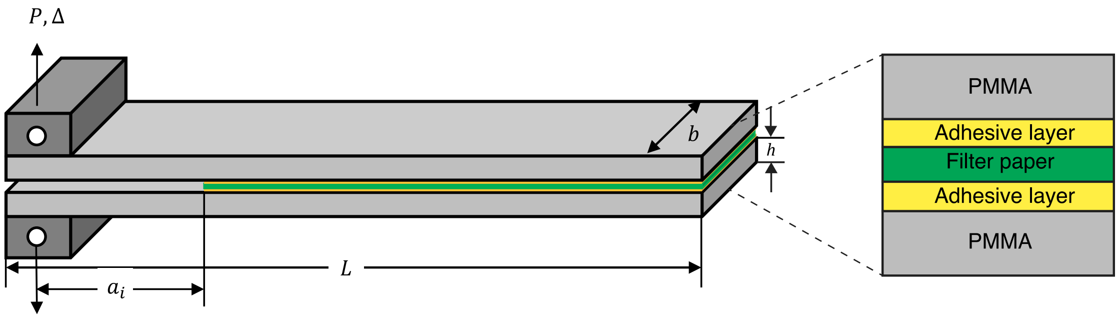

Fig. 1. Schematic of the DCB specimen in this study.

host of parameters for the fibers and bonds. For these reasons, and since we do not have control over individual fiber and fiber–fiber bonds properties in cellulose networks, we describe the fracture behavior through continuum traction-separation laws.

The paper is organized as follows: In Section 2 and Section 3, we discuss the materials, methods, and theory used in this study. The results of the experiments and simulations, and related discussion, is provided in Section 4. Finally, the main conclusions are discussed in Section 5.

2. Materials and methods

2.1. Materials

Commercial poly(methyl methacrylate) (PMMA) sheets (Curbell Plastics, Inc.), hydrophobic in nature [43], with thickness 2.85–3.05 mm were used as the top and bottom beams of the DCB. GE Whatman Grade-1 Filter Paper (Sigma Aldrich Inc.) with a nominal thickness of 170 micrometers is the cellulose network that is studied. Whatman filter paper was chosen since its manufacturing process is well established, so the properties of commercially available Whatman paper are relatively consistent. Additionally, Whatman filter paper is 100% cellulose, thicker, and weaker than commercial copy paper, so there is a greater chance of the crack propagating entirely through the paper and not shifting to an interface. Copy paper also contains inorganic materials to increase brightness and surface smoothness. The filter paper was bonded to the PMMA beams using Loctite 409 (McMaster Inc.). The thickness of the adhesive layer was carefully controlled to ensure that it did not fully infiltrate the paper layer (details below).

2.2. Conditioning and specimen preparation

If the relative humidity (RH) approaches a particular value from a lower RH (adsorption), the paper contains less water than if approached from a higher value (desorption). This hysteresis is well known in the paper industry. Since the direction from which a particular RH is approached plays an important role, it is a standard practice to convert relative humidity to moisture content. Here, the humidities 23%, 37%, 50%, and 75% are approached along an adsorption isotherm and 16% RH is achieved along a desorption isotherm. The filter paper specimens were conditioned for 48 h at every humidity at room temperature before measuring the mass of the specimens. These paper specimens were then adhered to the PMMA substrates and left in the humidity chamber for another 48 h before testing. The dry weight of the specimens was measured by placing the filter papers in a vacuum oven at 50 °C for 48 h. Moisture content is measured as Eq. (1).

$$mc = \frac{m_w - m_d}{m_d} * 100 \tag{1}$$

where m_d is the mass of the dry specimen, m_w is the mass of filter paper specimens at a particular RH, and mc is the moisture content.

The PMMA beams that were used in the DCB have a width of 9.5–10 mm and length of 70 mm. The beams are laser cut (Universal Laser PLS 4.75 flatbed laser cutter) from PMMA sheets of thickness 2.85–3.05 mm. After multiple trials using multiple adhesives and epoxies, thin pressure sensitive adhesives, and a thick 3M VHB tape, 70% wt./wt. Loctite 409 in acetone was determined to be the optimum composition of the adhesive to bond filter paper and the PMMA beams. This particular adhesive solution was strong enough to hold the filter paper between the two beams, thin enough to not penetrate into the filter paper, and sufficiently stiff to not deform meaningfully and affect measurements. An adjustable thin film coating applicator (Futiantian Technology Co., Ltd., China) is used to generate adhesive coatings of thickness 10 micrometers on PMMA surfaces. Samples were scrutinized both under optical microscope and SEM images to verify that the adhesive did not penetrate into the filter paper. An initial crack of length $a_i \approx 27$ mm is obtained by placing the filter paper at a distance of 30 mm from the beginning between the beams (see Fig. 1).

2.3. Out-of-plane tensile test

Cellulose fibrous networks have out-of-plane modulus and strength typically an order of magnitude (or two) less than the in-plane properties. As shown in the schematic in Fig. 3(a), filter paper is held in between two aluminum loading blocks using double-sided Norton polyurethane foam tape (1 mm thick). The aluminum blocks (5 mm × 5 mm) are mounted onto the machine using single pin joints on the top and bottom to help with self-correcting any misalignment during the test. Peak stress/traction of filter paper in the out-of-plane direction is calculated from the maximum measured force during the test. A uniaxial testing machine in displacement control (Criterion Model 43, MTS) was used for all mechanical testing. A displacement rate of 1 mm/min is used in the tests. Since most of the displacement applied deforms the foam tapes, optical measurements were performed (on the machine direction (MD) edge of the specimen) to measure the initial strain; from this strain and the measured stress the modulus was calculated. The tests are recorded at 30 frames per second, and up to 200 frames are used to calculate strain (eg. strain at 200^{th} frame = 4.2 ± 1.0%). The images were converted to grayscale images and line profiles of pixel intensity were extracted at 4 different locations to measure deformation of the paper during the test. The width at the average half peak intensity was measured in all images and used to calculate strain by comparing the average thickness to the one from the first frame.

2.4. Double cantilever beam testing

Double cantilever beam (DCB) tests were performed to determine the out-of-plane fracture toughness of the filter paper when the crack runs in the machine direction (MD). A displacement rate of 1 mm/min is used in all the tests. The load is applied to loading blocks adhered to the PMMA beams. From the loading cycle, the applied load versus displacement curve was obtained, and the crack length a and the strain energy release rate G were calculated using the following equations obtained by modifying (for different beam and foundation materials) the augmented double cantilever approach by Kanninen [44]:

$$a = \left(\frac{CE'bh^3}{8}\right)^{1/3} - \xi \tag{2}$$

$$G = \frac{12P^2a^2}{E'b^2h^3}\left(1+\xi\frac{1}{a}\right)^2 \tag{3}$$

$$\xi = \left(\frac{h^3h_f}{6}\frac{E'}{E_f}\right)^{\frac{1}{4}}, \tag{4}$$

where h is the thickness of each PMMA beam, b is the width of the beam, E' is the plane-strain modulus of the beam, h_f is the thickness of the Whatman paper foundation material, E_f is the out-of-plane modulus of the Whatman paper foundation material, C is the compliance of the elastic specimen measured from the force–displacement curve, and P is the applied load.

3. Theory and calculations

3.1. Cohesive zone model, traction- separation law, critical energy release rate, and non-dimensional parameter

Cohesive zone models have been shown to be effective at describing adhesion and fracture at material interfaces [45,46]. Since we have a thin sample of cellulose material in which the crack moves straight ahead in a one-dimensional manner, we use cohesive zone models to study crack propagation in our Whatman filter paper specimens.

The specimen and loading conditions were designed to maintain mode I fracture and to prevent shear loading at the interface. As such, the shear stress is negligible, and only the normal traction t_n must be considered. Therefore, similar to the derivation in [46], from initial stress until final failure, there are two regions characterized by the presence or absence of damage: the opening region before damage initiation, and the softening region after damage initiation until final failure. In the opening region the traction-separation law is linear-elastic:

$$t_n = K_n\delta_n, \tag{5}$$

where K_n is the stiffness in the normal direction and δ_n is the displacement. Once the traction reaches the critical value t_n^0 at displacement $\delta_n^0 = t_n^0/K_n$, damage initiation occurs. Then, in the softening region, the damage evolves as the traction predicted by the traction-separation law in the linear-elastic region multiplied by the damage parameter $(1-D)$. With a linear damage parameter

$$(1-D) = \left(\frac{\delta_n^0}{\delta_n}\right)\left(\frac{\delta_n^f-\delta_n}{\delta_n^f-\delta_n^0}\right), \tag{6}$$

where δ_n^f is the normal displacement to failure, the traction-separation law in the softening region becomes

$$t_n = K_n\delta_n^0\left(\frac{\delta_n^f-\delta_n}{\delta_n^f-\delta_n^0}\right). \tag{7}$$

Thus, the complete traction-separation law with linear softening is

$$t_n = \begin{cases} K_n \delta_n, & 0 \le \delta_n \le \delta_n^0 \\ K_n \delta_n^0 \left(\frac{\delta_n^f - \delta_n}{\delta_n^f - \delta_n^0} \right), & \delta_n \ge \delta_n^0, \end{cases} \tag{8}$$

where

$$\delta_n^0 = \frac{t_n^0}{K_n}, \tag{9}$$

with the following parameters: t_n^0, the critical normal traction, peak stress, or cohesive strength of the cellulose network; K_n, the normal stiffness; and δ_n^f, the displacement to failure.

With an exponential damage parameter

$$(1 - D) = \left(\frac{\delta_n^0}{\delta_n} \right) \left(1 - \frac{1 - \exp\left[-\alpha \left(\frac{\delta_n - \delta_n^0}{\delta_n^f - \delta_n^0} \right) \right]}{1 - \exp(-\alpha)} \right), \tag{10}$$

where δ_n^f is once again the normal displacement to failure and α is the exponential parameter, the traction-separation law in the softening region becomes

$$t_n = K_n \delta_n^0 \left(1 - \frac{1 - \exp\left[-\alpha \left(\frac{\delta_n - \delta_n^0}{\delta_n^f - \delta_n^0} \right) \right]}{1 - \exp(-\alpha)} \right). \tag{11}$$

Thus, the complete traction-separation law with exponential softening is

$$t_n = \begin{cases} K_n \delta_n, & 0 \le \delta_n \le \delta_n^0 \\ K_n \delta_n^0 \left(1 - \frac{1 - \exp\left[-\alpha \left(\frac{\delta_n - \delta_n^0}{\delta_n^f - \delta_n^0} \right) \right]}{1 - \exp(-\alpha)} \right), & \delta_n \ge \delta_n^0, \end{cases} \tag{12}$$

where the parameters t_n^0, K_n, and δ_n^f are the same as in the traction-separation law with linear softening (Eq. (8)), and α is the exponential parameter governing the shape of the exponential softening.

The toughness, or critical energy release rate, is the area under the traction-separation law curve and it can be expressed in terms of the previously defined parameters as [47–50]:

$$G_{Ic} = \int_0^{\delta_c} t_n d\delta_n. \tag{13}$$

Consistent with previous work [46,51], a non-dimensional parameter (NDP) is constructed to enable comparison between materials:

$$NDP = \frac{E_{PMMA} G_{Ic}}{\left(t_n^0\right)^2 h}. \tag{14}$$

The NDP is a measure of the toughness of a material: the lower the NDP, the tougher the material.

3.2. Finite element analysis

Finite element (FE) modeling and analysis was used to find the force–displacement curves corresponding to the cohesive parameters of different relative humidities. FE analysis was performed using the commercial software ABAQUS\Standard (Dassault Systèmes Simulia Corp) using a 2D plane strain model. The PMMA beams have length 67 mm and height 2.86 mm, and the Whatman filter paper has length 40 mm and height 171 μm. The Whatman filter paper region was aligned with the free end of the PMMA rectangular regions to give a pre-crack length of 27 mm (see Fig. 2). Displacement controlled vertical loading was applied at the top and bottom corners of the PMMA beams (see Fig. 2), and the inner corners of the PMMA beams are fixed in the horizontal direction. The PMMA beams were modeled as CPE4 plane strain elements, with Young's modulus 2.016 GPa to include both the contribution from the PMMA itself and the layer of Loctite adhering the Whatman filter paper to the PMMA beams, and Poisson's ratio $\gamma = 0.4$ (see Figure 1 in the Supplementary Material for a brief discussion of element types). The Whatman filter paper was modeled as a single row of COH2D4 cohesive elements with material properties captured by the cohesive parameters. The mesh was refined closer to the COH2D4 cohesive elements, and through a mesh convergence study, the number of elements in the mesh was selected to be approximately 22,000. This method of using cohesive elements with uniform properties is a standard technique to model the fracture of materials.

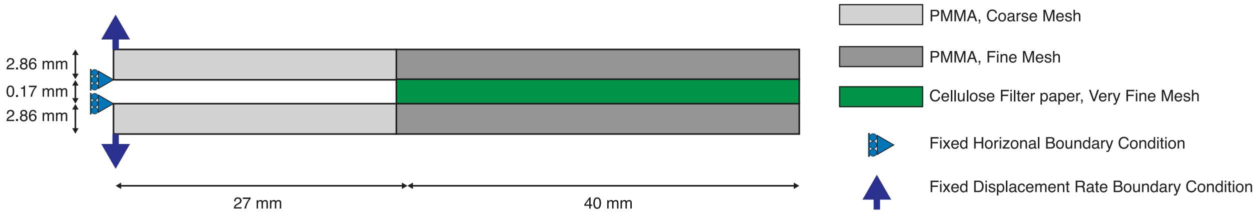

Fig. 2. Diagram of the part, partitions, and mesh density used in the finite element simulations. Also depicted are the length and height dimensions (not drawn to scale), as well as the locations of the loading (purple arrows) and fixed boundary (blue triangles) conditions.

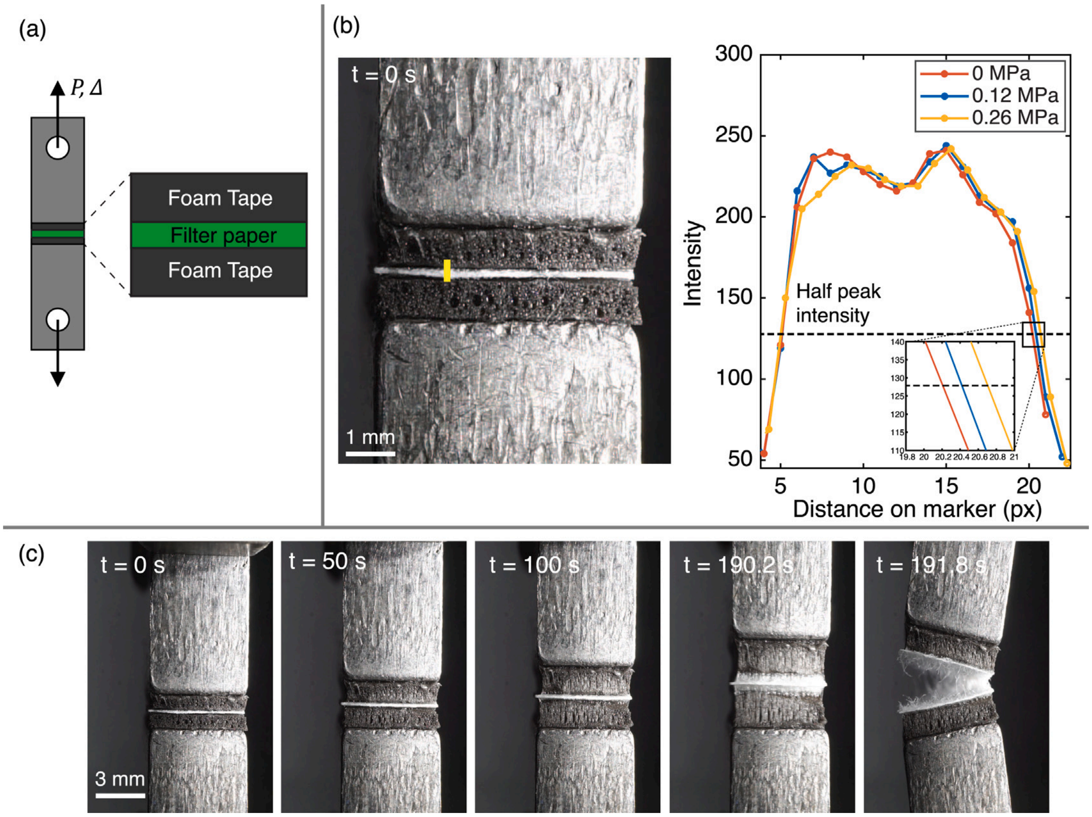

Fig. 3. (a) Schematic of the tensile specimen to measure out-of-plane mechanical properties. (b) Intensity profile of gray scale image at 16% RH at $t = 0$ s at the first location across the tape and filter paper. Dotted lines in the plot represent the half peak intensity. The thickness of the filter paper is the average of the width of regions where half peak intensity line intersect the intensity profiles. (c) Images taken during tests at 16% RH with times marked; test was performed at 1 mm/min.

4. Results and discussion

4.1. Out-of-plane modulus

Fig. 3(c) shows frames at various times during the test. To calculate the initial strains and therefore initial modulus, up to 200 frames (6.6s or 0.11 mm) are used in the analysis. The images are converted to gray scale and intensity profiles are extracted at four locations on each image. To consistently determine the deformations across the four markers, half peak intensity width is measured and the average value is used as the effective thickness of filter paper in that particular frame (shown in Fig. 3(b)). Strains are then calculated by comparing the average thicknesses to that from the initial frame. Moreover, it can be observed from Fig. 3(c) that the failure occurs inside the filter paper, so the peak force during the test can be used to estimate the peak stress/traction for the filter paper. This value of peak traction is later used in the cohesive zone models in the numerical analysis. The out-of-plane tensile experiments were performed at 16% RH (room condition), and at 50% RH and 75% RH. Modulus and traction values are interpolated for 23% RH and 37% RH by plotting a graph of $ln(E)$ as a function of moisture content mc [40,52,53]. The out-of-plane peak stress/traction for 23% RH and 37% RH were interpolated linearly between 16% RH and 50% RH.

Table 1
Summary of out-of-plane toughness values of filter paper as a function of humidity. Two or three experiments were performed for each RH, and the results are given in the form $X \pm Y$, where X represents the mean value and Y represents the standard deviation.

Humidity	Moisture Content (%)	Young's modulus E(MPa)	Toughness G_{Ic}(J/m^2)
16% RH	2.71	6.41 ± 1.75	16.34 ± 1.19
23% RH	3.17	5.57	12.90 ± 1.16
37% RH	4.05	4.28	9.27 ± 2.55
50% RH	5.11	3.12 ± 0.85	7.26 ± 0.65
75% RH	9.03	0.86 ± 0.34	2.32 ± 0.56

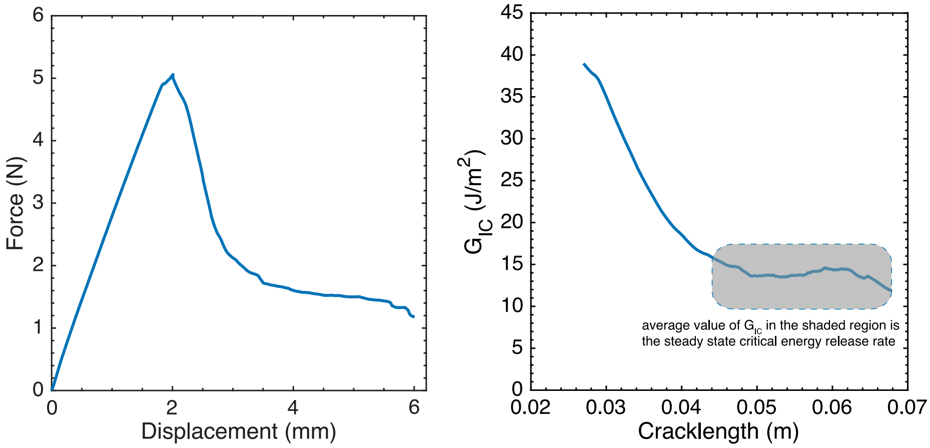

(a) Force versus Displacement (b) Energy Release Rate versus Crack length

Fig. 4. Representative Force–Displacement and subsequent Energy Release Rate plots at 23% RH from a DCB specimen.

4.2. Experimental critical energy release rate

Force versus displacement data obtained from the loading of DCB specimens is used to calculate crack length a and energy release rate G from the compliance model using modified beam theory given by Eq. (2) and (3). Fig. 4 shows an example force–displacement curve and G_C as a function of the crack length a calculated from this curve. G is not defined when $a < a_i$. The energy release rate decreases as the crack grows ($a > a_i$) and stabilizes over a set of crack lengths as the crack propagates. The average energy release rate in the steady state region (gray shaded region) is taken as the critical energy release rate G_c. This value is representative of the toughness of a sharp crack tip in a uniform material; the initial crack tip here is blunt, and there are other factors as well such as artificial compression induced by the scissor cut at the edge, which is why the initial energy release rate is higher than the steady state value. This is a commonly observed phenomenon in the absence of sharp crack or some other artifact at the pre-crack in a DCB configuration, as reported by River and Okkonen [54] who categorized the quantities as crack initiation energy and crack arrest energy, and as explained by Long and Hui [55] who depicted why the assumption of translational invariance, or steady-state crack growth, does not hold in the crack initiation region using the example of hydrogels. In principle, especially for soft materials and for materials with no sharp crack, an extra term of stress and deformation fields due to crack initiation must be included in G.

Table 1 shows the variation of critical energy release rate as a function of moisture content. As moisture content increases, the toughness of the paper decreases, which is expected due to the weakening of the individual cellulose fibers and the bonds between them. This behavior of modulus with moisture content was also observed in similar earlier works [40,52,53,56,57].

4.3. Finite element modeling results

4.3.1. Exponential vs. Linear softening

Simulations for 23% relative humidity were run with both linear softening Eq. (8) and exponential softening Eq. (12), to determine which traction-separation law fit best with the experimental results (Figure 2 in the Supplementary Material). As can be seen in Figure 2 in the Supplementary Material, the results from both simulations were almost identical. As such, the traction-separation law with linear softening Eq. (8) was chosen for the remainder of the simulations because it has fewer parameters and has a slight advantage in terms of the speed of simulations.

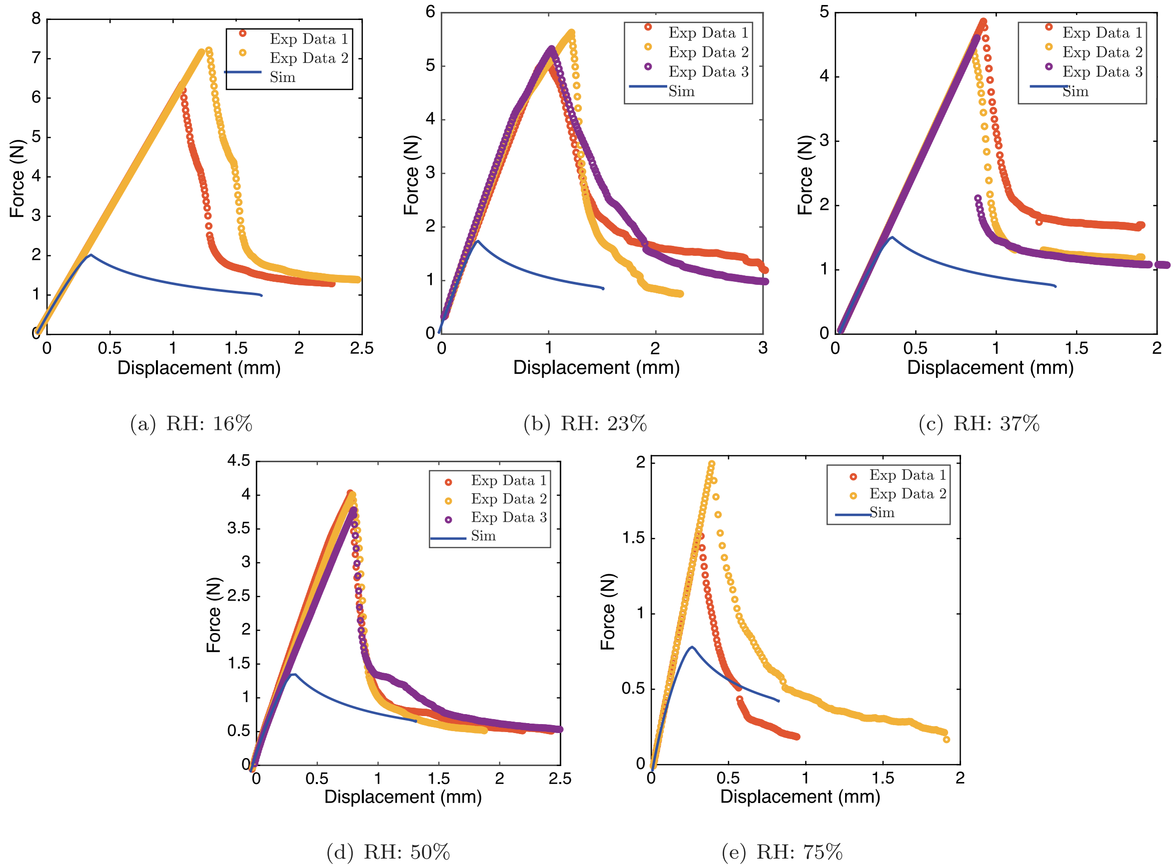

Fig. 5. Force–displacement plots from simulations (solid curves) as compared with experimental data (hollow circles) at different relative humidities (a) 16% RH, (b) 23% RH, (c) 37% RH, (d) 50% RH, and (e) 75% RH.

Table 2
Simulation parameter values by humidity for which force–displacement plots from simulations at different relative humidities best fit with the corresponding force–displacement plots from experiments.

%RH	K_0 (10^{10} Pa/m)	t_n^0 (MPa)	δ_f (μm)	G_{Ic} (J/m^2)	NDP (unit-less)	F_{max} (N)
16	3.77	0.800	19.63	16.34	17.00	1.94
23	3.28	0.600	24.69	12.90	23.86	1.86
37	2.52	0.400	30.46	9.27	38.57	1.64
50	1.84	0.310	29.95	7.26	50.31	1.41
75	0.51	0.075	47.04	2.32	274.64	0.81

4.3.2. Parameters for different relative humidities

The parameters for the simulations were selected in the following manner. t_n was chosen as the measured peak stress from the out-of-plane tensile tests Section 4.1 . K_0 was chosen as

$$K_0 = \frac{E_f}{h_f}, \tag{15}$$

based on the out-of-plane modulus E_f of the filter paper from the out-of-plane tensile tests Section 4.1 and the thickness of the filter paper h_f. δ_f was then chosen such that the resulting toughness value Eq. (13) from the traction-separation law Eq. (8) was within the uncertainty range of the toughness values from the experimental data. Finally, NDP was calculated using Eq. (14).

The parameters for which the force–displacement plots from simulations of different relative humidity (Fig. 5) best fit with the corresponding force–displacement plots from experiments are listed in Table 2, and the peak stresses t_n^0 and displacements δ_c and δ_f are plotted vs. humidity in Fig. 6(a).

Fig. 6(b) shows the traction-separation laws with linear softening (Eq. (8)) for the different relative humidities. The toughness, or critical energy release rate, value from the simulations is found by calculating the area under the traction-separation curve (Eq. (13)).

As can be seen in Fig. 5, the initial loading portion of the simulations and the unloading stable crack growth regions fit well with the experimental data, but the simulations do not capture the large peak force and sudden drop which are present in the plots from

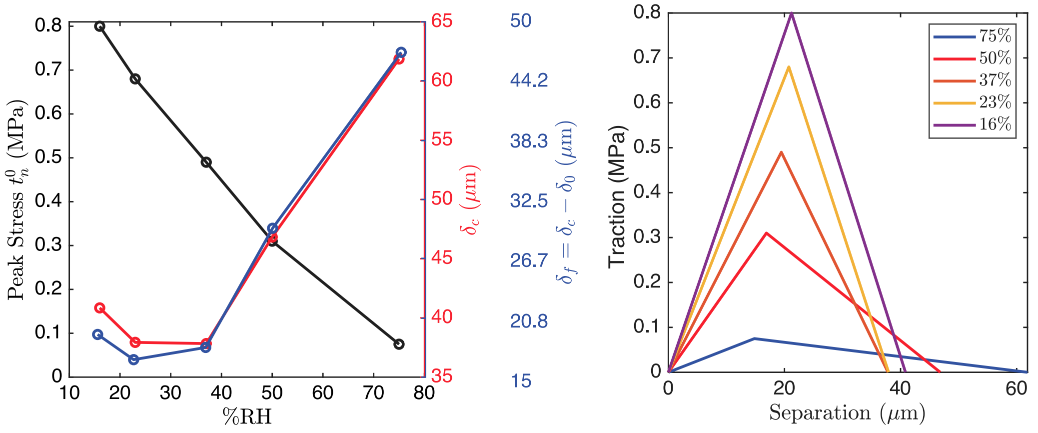

(a) Parameters vs. %RH (relative humidity).

(b) Traction-separation law plots from simulations at different relative humidities.

Fig. 6. Cohesive parameters and cohesive law at different relative humidities: (a) Plots of the parameters peak stress t_n^0, and displacements δ_f and δ_c vs. %RH (relative humidity), and (b) Traction-separation law plots from simulations at different relative humidities, using the traction-separation law with linear softening (Eq. (8)).

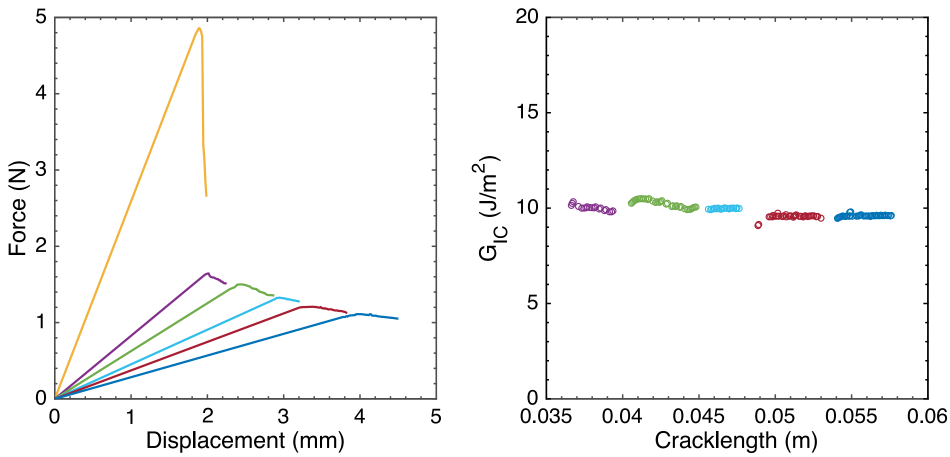

(a) Force vs Displacement

(b) Critical Energy Release Rate

Fig. 7. Force–displacement data of a multiple loading DCB test of filter paper at 31% RH.

the experimental data. The reason that these simulations cannot capture the peak force and sudden drop from the experimental results is, as mentioned earlier in Section 4.2, that the Whatman filter paper in the experiments does not have a sharp crack, and the crack must be initiated before fracture mechanics applies [54,55]. We also considered other possibilities, such as compressive stresses far ahead of the crack and non-uniform drying. Since there is compression ahead of the cohesive zone as can be seen in Figure 3 in the Supplementary Material, the cellulose network ahead of the crack could be damaged by the compression [55,58–60] and could have a lower toughness than the initial region which is only subject to tension. Additionally, the specimens are cut to the required sizes using scissors which could potentially induce an artificial compression at the edge (pre-crack), which increases the resistance to the crack propagation at the pre-crack tip.

From Figure 3 in the Supplementary Material it can be observed that the maximum compressive stress ahead of the crack is around 0.55 MPa for the 16% RH and 0.15 MPa for the 75% RH. From Table 1, the out-of-plane Young's modulus of the filter paper at 16% RH is 6.41 MPa and at 75% RH is 0.86 MPa. Hence, the compressive strain in the cellulose fibers ahead of the crack tip is around 0.55/6.41 = 0.086 for 16% RH and 0.15/0.86 = 0.17 for 75% RH. Buckling typically starts around compressive strain of 0.05 in foams and fiber networks [61], which is smaller than the compressive strains calculated above. However, the compressive stiffness is likely higher than the tensile stiffness, especially because compressing porous fibrous networks causes an increase in density which therefore could increase compressive stiffness [62,63], and this could likely lower the calculated compressive strains.

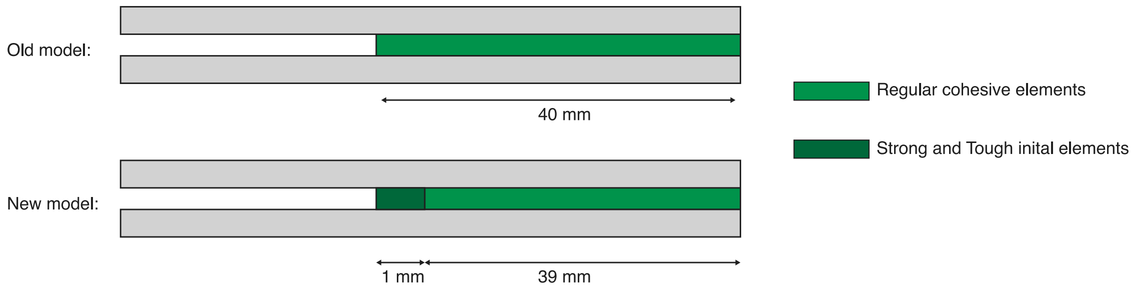

Fig. 8. Cartoon depicting the changes made to the model in order to incorporate the tougher initiation region cohesive elements, as well as the regular cohesive elements. (Note: This image is not to scale.).

Table 3
Simulation parameter values by humidity for which force–displacement plots from simulations including the initiation element region at different relative humidities best fit with the corresponding force–displacement plots from experiments.

%RH	Element Type	K_0 (10^{10} Pa/m)	t_n^0 (MPa)	δ_f (μm)	G_{Ic} (J/m^2)	NDP (unit-less)	F_{max} (N)
16	Initiation Cohesive Elements	781.77	8.000	21.36	89.50	0.93	6.41
	Steady State Cohesive Elements	3.77	0.800	19.63	16.34	17.00	
23	Initiation Cohesive Elements	692.94	6.000	19.14	59.98	1.11	5.04
	Steady State Cohesive Elements	3.28	0.600	24.69	12.90	23.86	
37	Initiation Cohesive Elements	517.65	4.000	20.22	41.98	1.75	3.70
	Steady State Cohesive Elements	2.52	0.400	30.46	9.27	38.57	
50	Initiation Cohesive Elements	255.29	3.100	20.84	34.18	2.39	3.05
	Steady State Cohesive Elements	1.84	0.310	29.95	7.26	50.31	
75	Initiation Cohesive Elements	55.41	0.750	16.59	6.73	7.96	1.03
	Steady State Cohesive Elements	0.51	0.075	47.04	2.32	274.64	

Moreover, the peak compressive stress/strain is millimeters ahead of the crack tip before the crack starts to propagate, whereas the sudden drop from peak force happens even before the crack starts to propagate. Additionally, the compressive strain limit of 0.05 in general foams and fiber networks [61] is valid for 3D isotropic materials. This is not necessarily the limit for cellulose networks, in particular filter paper, which are non-isotropic materials and most of the fibers are not aligned in the out-of-plane direction of loading. This implies that the presence of compressive stresses ahead of the crack tip may not be a significant factor contributing to the force anomaly.

To study the impact of artifacts at the pre-crack, such as having a blunt crack or scissors-induced compression, a new type of experiment was done at one humidity (31% RH) with multiple loading–unloading cycles. The phenomenon of initial high peak force and sudden drop can be clearly isolated (as shown in Fig. 7(a)) from the region of stable crack growth using the equation resulting in a flat R-curve (as shown in Fig. 7(b)) using (2) and (3). This experiment shows that among the reasons causing the initial high peak force, artifacts at the pre-crack, such as having a blunt crack or scissors-induced compression are the primary reason for the force anomaly and further corroborates that compression ahead of the crack-tip is not a significant factor.

Inspired by a previous report [55], to account for the change in behavior from crack initiation to crack propagation, cohesive elements representing the Whatman paper are divided into two regions: a crack initiation region with parameters that give higher toughness, and the steady state crack growth region comprising the rest of the Whatman filter paper with parameters estimated before (see Fig. 8). We choose a length for this crack initiation region to be 1 mm since this is about 10 times larger than the root radius of the initial crack. We choose the cohesive parameters for this initiation region by using the following process: First, as the toughness value we take the maximum energy release rate in the experimental data (as calculated by Eq. (3)). We choose the peak stress t_n^0 to be exactly one order of magnitude larger than in the steady state region, and we choose the stiffness K_0 to be about two orders of magnitude larger than in the steady state region. We calculate the displacement to failure δ_f parameter from the toughness relation Eq. (13), and NDP from Eq. (14).

As can be seen in Fig. 9, the simulations including the initiation region to represent the apparent toughness due to the artifacts at the pre-crack, such as having a blunt crack or scissors-induced compression, capture not only the initial loading portion and the steady state crack growth region of the unloading portion of the force–displacement curves, but also the peak force and the sudden drop. The transition between the initiation region and steady state crack growth region is known to be complex [55], so we do not model it here. The parameters of the simulations using the initiation region model for which the force–displacement plots from simulations of different relative humidities (Fig. 9) best fit with the corresponding force–displacement plots from experiments are listed in Table 3. There is some variability in the experimental data, and small variations in the thickness and modulus of the PMMA have a large effect on the energy release rate (see Eq. (3)) so the fits are not exact, but the key qualitative features of the force–displacement curve can be explained by the presence of an initiation region to represent the apparent toughness due to

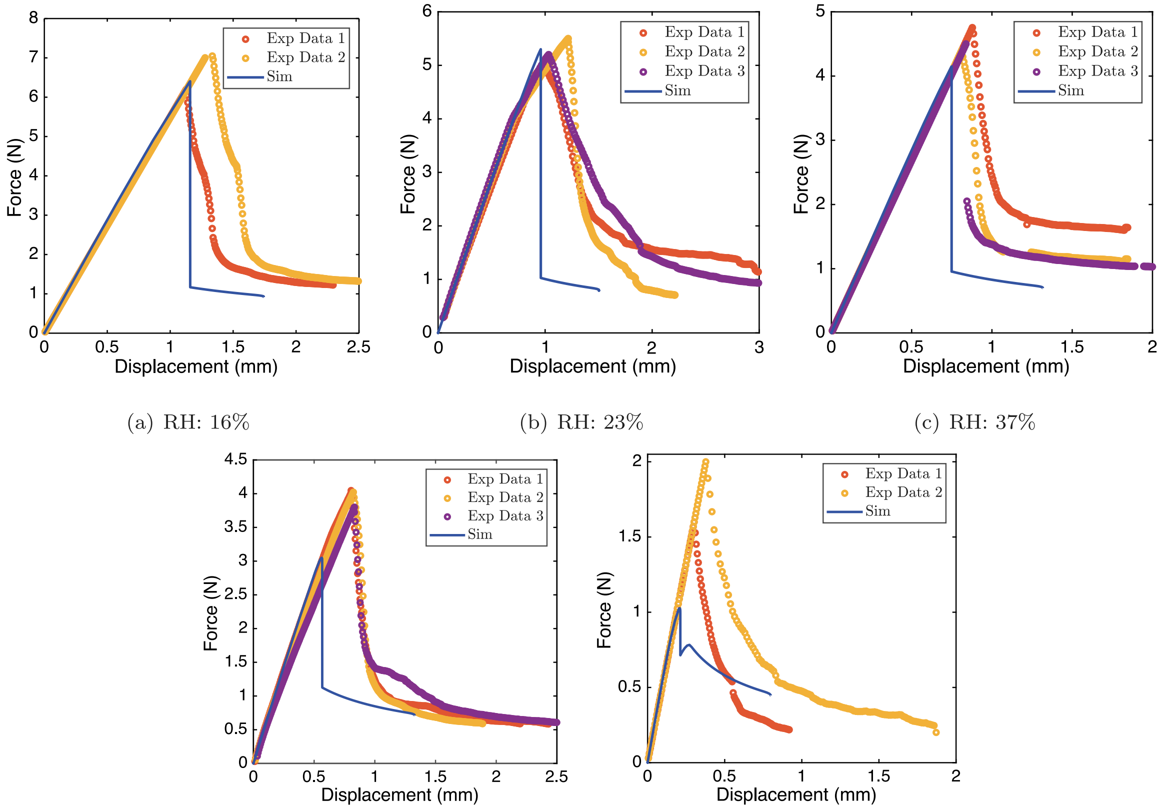

(a) RH: 16%

(b) RH: 23%

(c) RH: 37%

(d) RH: 50%

(e) RH: 75%

Fig. 9. Force–displacement plots from simulations including the tougher cohesive element crack initiation regions (solid curves) as compared with experimental data (colored circles) at different relative humidities (a) 16% RH, (b) 23% RH, (c) 37% RH, (d) 50% RH, and (e) 75% RH.

the pre-crack artifacts in our finite element calculations (see Figure 4 in the Supplementary Material for verification that both the initiation region and steady state region are necessary to capture the experimental results) .

The results shown here with the high peak force and sudden drop to a plateau region of steady state crack growth, both in experiments and simulations, resemble results from earlier works such as [54]. Depicted there is a plot for three different materials exhibiting the same behavior with an initial high peak force and then a sudden drop to a lower plateau (see Figure 11 in [54]). However, these plots exhibit a saw-tooth pattern due to a boundary condition of holding opening displacement of the DCB fixed in cycles. This is not seen in our experimental results since we continuously increase the opening displacement of our DCB, not doing so in a step-wise fashion. In our simulations the opening displacement is increased in a step-wise fashion but those steps are small so that it mimics a continuous increase. Nonetheless, it is clear that there is a direct analogy between the crack initiation energy in [54] and our initiation region toughness value G_{Ii}, and between the crack arrest energy in [54] and our steady state crack growth region toughness value G_{Ic}.

Generally, it is preferable to design experiments in such a way that either a sharp crack is produced before any measurements are taken or precautions are taken to make sure the material is uniform throughout the length, to avoid high peaks and sudden drops in the force–displacement data. However, in some systems it is difficult to introduce a sharp crack initially, such as in [54] or when studying the fracture toughness of the out-of-plane direction of two-dimensional sheets as we do here. Our simulation approach which includes an initial crack initiation region with tougher/stronger cohesive elements to represent the apparent toughness due to artifacts, followed by steady-state crack growth region cohesive elements accounts for this difficulty in the experiment and allows for extraction of useful data even in such situations in which experimentally obtaining a sharp crack is difficult or even impossible.

4.3.3. Parametric study

In studying the effect on the force–displacement plot of each of the five different parameters in the bi-linear traction-separation law, it is important to keep in mind that only three of them can be independent for any given simulation. For example, the parameter G_{Ic} defined above (Eq. (13)) for the bi-linear traction-separation law Eq. (8) can be rewritten as

$$G_{Ic} = \frac{t_n^0}{2}\left(\frac{t_n^0}{K_n} + \delta_f\right), \tag{16}$$

Table 4
Toughness values calculated from simulations at different relative humidities and the corresponding values as measured from experiments. The experimental results are given in the form $X \pm Y$, where X represents the mean value and Y represents the standard deviation. The toughness values calculated from the simulation results for all five relative humidities are within the measurement errors of the toughness values measured from the experimental data.

RH:	16%	23%	37%	50%	75%
Simulation G_{I_c} (J/m^2):	16.33	12.90	9.27	7.26	2.32
Experiment G_{I_c} (J/m^2):	16.34 ± 1.19	12.90 ± 1.16	9.27 ± 2.55	7.26 ± 0.65	2.32 ± 0.56

and therefore the parameter NDP defined above (Eq. (14)) can also be rewritten

$$NDP = \frac{E_{PMMA}}{2h}\left(\frac{1}{K_n} + \frac{\delta_f}{t_n^0}\right), \tag{17}$$

both now entirely in terms of cohesive properties t_n^0, K_n, and δ_f. Alternatively, the above equations Eq. (16) and (17) can be rearranged into

$$t_n^0 = \sqrt{\frac{E_{PMMA}G_{Ic}}{h\ NDP}} \tag{18}$$

$$\delta_f = \sqrt{\frac{E_{PMMA}G_{Ic}}{h\ NDP}}\left(\frac{2h\ NDP}{E_{PMMA}} - \frac{1}{K_n}\right), \tag{19}$$

such that the cohesive parameters δ_f and t_n are entirely in terms of cohesive parameters K_n, G_{Ic}, and NDP. The latter three are the ones we use in our parameter study below.

As can be seen in Figure 5(a) in the Supplementary Material, a 10% change in the K_0 value, both higher and lower, has no visible effect on the force–displacement plots. The 10% lower $K_0 = 5.91 * 10^{12}$ Pa/m yields a slightly lower peak force of 5.37 N and pulls the sudden drop to a slightly lower displacement of 0.968 mm, and vice versa for the 10% higher K_0. Similarly, as can be seen in Figure 5(b) in the Supplementary Material, a 10% change in the NDP parameter has little visible effect; a 10% lower $NDP = 0.90$ yields a slightly higher peak force of 5.41 N and pushes the sudden drop to a slightly higher displacement of 0.98 mm, and a 10% higher $NDP = 1.10$ yields a slightly lower peak force of 5.34 N and pulls the sudden drop to a slightly lower displacement of 0.96 mm, both as compared to the $NDP = 1.00$ with a peak force of 5.39 N and sudden drop at a displacement of 0.97 mm. (Larger changes in NDP may have more significant effects.) However, as can be seen in Figure 5(c) in the Supplementary Material, a 10% change in the G_{Ii} parameter has a much more significant effect on the force–displacement plots; a 10% lower $G_{Ii} = 52.79$ J/m^2 yields a lower peak force of 5.11 N and pulls the sudden drop to a lower displacement of 0.92 mm, and a 10% higher $G_{Ii} = 64.54$ J/m^2 yields a higher peak force of 5.62 N and pushes the sudden drop to a higher displacement of 1.01 mm, both as compared to the $G_{Ii} = 58.62$ J/m^2 with a peak force of 5.39 N and sudden drop at displacement 0.97 mm.

It should also be noted that, as expected, for each of the simulations, the toughness value is (approximately) directly proportional to the square of the peak force value:

$$G_{Ii} \approx 2F_{\max}^2. \tag{20}$$

4.3.4. Comparison of experiments and simulations

As can be seen in Fig. 9, the force–displacement plots obtained from the finite element calculations with linear softening and tougher initiation region fit the experimental data quite well. For example, for 16% relative humidity in Fig. 9(a), the loading slopes from the experimental data and the simulation results are almost identical, the peak forces are very close, and the unloading curves are similar in shape and magnitude, including the sudden drop from the peak force and its location in the plot. The same is true for 23% relative humidityṪhe peak forces are less close in (Fig. 9(b)), 37% relative humidity (Fig. 9(c)), 50% relative humidity (Fig. 9(d)), and 75% relative humidity (Fig. 9(e)), but all other characteristics of the experiment are captured. It should be noted that small variations in the thickness and modulus of the PMMA have a large effect on the energy release rate (see Eq. (3)) so the fits are not exact. Additionally, if the NDP in the initiation region is held fixed at 1 instead of specifying the peak stress there, the fits would improve (see Figure 6 in the Supplementary Material).

It should also be noted that the displacement value used here for comparison in both the experimental data and the simulation results is $\delta = \Delta/2$, or half of the distance between the two ends of the original crack tip, and not Δ, the full distance between the two ends of the original crack tip.

A comparison of the toughness values measured from experiments to those calculated from the simulation results for different relative humidities can be found in Table 4. The toughness values calculated from the simulation results for all five relative humidities are within the measurement errors of the toughness values measured from the experimental data.

The reader can also simultaneously look at Supplementary Material Video 1, to visualize the crack propagation during fracture in the experiment and simulation.

5. Conclusion

In the current study, the effect of moisture content on out-of-plane toughness of cellulose filter paper was studied using double cantilever beam fracture tests. Cohesive zone modeling was used to describe crack propagation in the filter paper. The parameters of the traction-separation laws were fitted to experimental data. Experimental measurements revealed a decreasing trend in the modulus and fracture toughness with an increase in moisture content, as a consequence of moisture induced weakening of cellulose network. Due to pre-crack artifacts, there is a higher peak force and sudden decrease as the crack grows, which was captured by the newly developed finite element model involving two kinds of cohesive elements: tough elements near the initial crack tip to represent the apparent toughness due to artifacts at the pre-crack, such as having a blunt crack or scissors-induced compression, succeeded by steady state crack growth elements. The effect of each independent cohesive parameter was also investigated, and the overall force–displacement curves of the DCB specimens was captured quite well.

CRediT authorship contribution statement

Russell Spiewak: Writing – review & editing, Writing – original draft, Visualization, Validation, Software, Resources, Methodology, Investigation, Formal analysis, Data curation, Conceptualization. **Gnana Saurya Vankayalapati:** Software, Validation, Visualization, Writing – original draft, Writing – review & editing, Conceptualization, Data curation, Formal analysis, Investigation, Methodology, Resources. **John M. Considine:** Writing – review & editing, Supervision. **Kevin T. Turner:** Conceptualization, Funding acquisition, Project administration, Resources, Supervision, Writing – review & editing. **Prashant K. Purohit:** Writing – review & editing, Supervision, Project administration, Funding acquisition, Conceptualization.

Declaration of competing interest

The authors declare that they have no known competing financial interests or personal relationships that could have appeared to influence the work reported in this paper.

Acknowledgments

RS was partially supported through a Department of Education GAANN fellowship grant number P200A160282 to the Department of Mechanical Engineering and Applied Mechanics at the University of Pennsylvania and an NIH grant R01 HL135254 to PKP. GSV was partially supported through a USDA AFRI grant 2017-67021-26601 to KTT.

Appendix A. Supplementary data

Supplementary material related to this article can be found online at https://doi.org/10.1016/j.engfracmech.2022.108330.

References

[1] Fukuzumi H, Saito T, Iwata T, Kumamoto Y, Isogai A. Transparent and high gas barrier films of cellulose nanofibers prepared by TEMPO-mediated oxidation. Biomacromolecules 2009;10(1):162–5. http://dx.doi.org/10.1021/bm801065u.

[2] Isogai A. Wood nanocelluloses: fundamentals and applications as new bio-based nanomaterials. J Wood Science 2013;59(6):449–59. http://dx.doi.org/10.1007/s10086-013-1365-z.

[3] Paunonen S. Strength and barrier enhancements of cellophane and cellulose derivative films: A review. BioResources 2013;8:3098–121. http://dx.doi.org/10.15376/BIORES.8.2.3098-3121.

[4] Schmied FJ, Teichert C, Kappel L, Hirn U, Bauer W, Schennach R. What holds paper together: Nanometre scale exploration of bonding between paper fibres. Sci Rep 2013;3:2432–8. http://dx.doi.org/10.1038/srep02432.

[5] Hirn U. Comprehensive analysis of individual pulp fiber bonds quantifies the mechanisms of fiber bonding in paper. Sci Rep 2015;5:10503. http://dx.doi.org/10.1038/srep10503.

[6] Tanaka A, Yamauchi T. Deformation and fracture of paper during the in-plane fracture toughness testing–examination of the essential work of fracture method. J Mater Sci 2000;35:1827–33. http://dx.doi.org/10.1023/A:1004797023064.

[7] Wanigaratne DMS. Investigation of an alternative technique to measure fracture toughness of paper [Ph.D. thesis], 2004.

[8] Tryding J, Marin G, Nygårds M, Mäkelä P, Ferrari G. Experimental and theoretical analysis of in-plane cohesive testing of paperboard. Int J Damage Mech 2017;26(6):895–918. http://dx.doi.org/10.1177/1056789516630776.

[9] Zechner J, Janko M, Kolednik O. Determining the fracture resistance of thin sheet fiber composites – Paper as a model material. Compos Sci Technol 2013;74:43–51. http://dx.doi.org/10.1016/j.compscitech.2012.10.007.

[10] Wanigaratne D, Batchelor W, Parker I. Comparison of fracture toughness of paper with tensile properties. In: 55th appita annual conference, Hobart, Australia 30 April-2 May 2001: Proceedings. Appita Inc.; 2001, p. 217–23.

[11] Golling S, Fròmeta D, Casellas D, Granström a, Jonsén P, Oldenburg M. Determination of the essential work of fracture at high strain rates. In: 6th international conference hot sheet metal forming of high-performance steel. Association for Iron & Steel Technology; 2017, p. 261–9.

[12] Zhu H, Zhu S, Jia Z, Parvinian S, Li Y, Vaaland O, et al. Anomalous scaling law of strength and toughness of cellulose nanopaper. Proc Natl Acad Sci 2015;112(29):8971–6. http://dx.doi.org/10.1073/pnas.1502870112.

[13] Mao R, Goutianos S, Tu W, Meng N, Yang G, Berglund LA, et al. Comparison of fracture properties of cellulose nanopaper, printing paper and buckypaper. J Mater Sci 2017;52(16):9508–19. http://dx.doi.org/10.1007/s10853-017-1108-4.

[14] Mäkelä P, Östlund S. Cohesive crack modelling of thin sheet material exhibiting anisotropy, plasticity and large-scale damage evolution. Eng Fract Mech 2012;79:50–60. http://dx.doi.org/10.1016/j.engfracmech.2011.10.001, URL https://www.sciencedirect.com/science/article/pii/S0013794411003687.

[15] Meng Q, Li B, Li T, Feng X-Q. A multiscale crack-bridging model of cellulose nanopaper. J Mech Phys Solids 2017;103:22–39. http://dx.doi.org/10.1016/j.jmps.2017.03.004, URL https://www.sciencedirect.com/science/article/pii/S0022509617300674.

[16] Onck PR, Koeman T, Van Dillen T, Van Der Giessen E. Alternative explanation of stiffening in cross-linked semiflexible networks. Phys Rev Lett 2005;95(17):178102. http://dx.doi.org/10.1103/PhysRevLett.95.178102.

[17] Žagar G, Onck PR, der Giessen EV. Elasticity of rigidly cross-linked networks of athermal filaments. Macromolecules 2011;44:7026–33. http://dx.doi.org/10.1021/ma201257v.

[18] Žagar G, Onck PR, der Giessen EV. Two fundamental mechanisms govern the stiffening of cross-linked networks. Biophys J 2015;108:1470–9. http://dx.doi.org/10.1016/j.bpj.2015.02.015.

[19] Deogekar S, Picu RC. On the strength of random fiber networks. J Mech Phys Solids 2018;116:1–16. http://dx.doi.org/10.1016/j.jmps.2018.03.026.

[20] Deogekar S, Islam M, Picu R. Parameters controlling the strength of stochastic fibrous materials. Int J Solids Struct 2019;168:194–202. http://dx.doi.org/10.1016/j.ijsolstr.2019.03.033.

[21] Deogekar S, Yan Z, Picu RC. Random fiber networks with superior properties through network topology control. J Appl Mech 2019;86(8):081010. http://dx.doi.org/10.1115/1.4043828.

[22] Deogekar S, Picu RC. Strength of stochastic fibrous materials under multiaxial loading. Soft Matter 2021;17:704–14. http://dx.doi.org/10.1039/D0SM01713B.

[23] Abhilash AS, Purohit PK, Joshi SP. Stochastic rate-dependent elasticity and failure of soft fibrous networks. Soft Matter 2012;8:7004–16. http://dx.doi.org/10.1039/C2SM25450F.

[24] Yun S, Kim JH, Li Y, Kim J. Alignment of cellulose chains of regenerated cellulose by corona poling and its piezoelectricity. J Appl Phys 2008;103:083301. http://dx.doi.org/10.1063/1.2908883.

[25] Yang C, Kim J-H, Kim J-H, Kim J, Kim HS. Piezoelectricity of wet drawn cellulose electro-active paper. Sensors Actuators A 2009;154:117–22. http://dx.doi.org/10.1016/j.sna.2009.07.016.

[26] Service RF. A battery made with paper: Nanotubes on photocopy paper could lead to cheap, flexible source of power. Amer Assoc Adv Sci: Sci 2009. http://dx.doi.org/10.1126/article.31438.

[27] Zeng L, Chen S, Liu M, Cheng H-M, Qiu L. Integrated paper-based flexible li-ion batteries made by a rod coating method. Am Chem Soc Appl Mater Interfaces 2019;11:46776–82. http://dx.doi.org/10.1021/acsami.9b15866.

[28] Östlund S, Nygårds M. Through-thickness mechanical testing and computational modelling of paper and board for efficient materials design. In: Hannu Paulapuro symposium. Esbo, Finland; 2009, p. 69–82.

[29] Nygårds M, Fellers C, Östlund S. Measuring out-of-plane shear properties of paperboard. J Pulp Pap Sci 2007;33(2):6.

[30] Nygårds M. Experimental techniques for characterization of elasticplastic material properties in paperboard. Nordic Pulp Pap Res J 2008;23(4):432–7. http://dx.doi.org/10.3183/npprj-2008-23-04-p432-437, URL https://www.degruyter.com/document/doi/10.3183/npprj-2008-23-04-p432-437/html.

[31] Nygårds M, Hallbäck N, Just M, Tryding J. A finite element model for simulations of creasing and folding of paperboard. In: ABAQUS user's conference. 2005, p. 1–15.

[32] Gamstedt EK. Moisture induced softening and swelling of natural cellulose fibres in composite applications. Mater Sci Eng 2016;012003. http://dx.doi.org/10.1088/1757-899X/139/1/012003.

[33] Célino A, Fréour S, Jacquemin F, Casari P. The hygroscopic behavior of plant fibers: a review. Front Chem 2014;1(43):1–12. http://dx.doi.org/10.3389/fchem.2013.00043.

[34] Jajcinovic M, Fischer WJ, Mautner A, Bauer W, Hirn U. Influence of relative humidity on the strength of hardwood and softwood pulp fibres and fibre to fibre joints. Cellulose 2018;25(4):2681–90. http://dx.doi.org/10.1007/s10570-018-1720-8.

[35] Placet V, Cisse O, Boubakar ML. Influence of environmental relative humidity on the tensile and rotational behaviour of hemp fibres. J Mater Sci 2012;47(7):3435–46. http://dx.doi.org/10.1007/s10853-011-6191-3.

[36] Alamri H, Low I. Mechanical properties and water absorption behaviour of recycled cellulose fibre reinforced epoxy composites. Polym Test 2012;31(5):620–8. http://dx.doi.org/10.1016/j.polymertesting.2012.04.002.

[37] Benítez AJ, Torres-Rendon J, Poutanen M, Walther A. Humidity and multiscale structure govern mechanical properties and deformation modes in films of native cellulose nanofibrils. Biomacromolecules 2013;14(12):4497–506. http://dx.doi.org/10.1021/bm401451m.

[38] Meng Q, Wang TJ. Mechanics of strong and tough cellulose nanopaper. Appl Mech Rev 2019;71(4):040801. http://dx.doi.org/10.1115/1.4044018.

[39] Moropoulou A, Zervos S. The immediate impact of aqueous treatments on the strength of paper. Restaurator 2003;24(3):160–77. http://dx.doi.org/10.1515/REST.2003.160, URL https://www.degruyter.com/document/doi/10.1515/REST.2003.160/html.

[40] Nissan AH. H-bond dissociation in hydrogen bond dominated solids. Macromolecules 1976;9(5):840–50. http://dx.doi.org/10.1021/ma60053a026, URL https://pubs.acs.org/doi/abs/10.1021/ma60053a026.

[41] Vitale T. Effects of water on the mechanical properties of paper and their relationship to the treatment of paper. MRS Proc 1992;267:397–427. http://dx.doi.org/10.1557/PROC-267-397, URL http://link.springer.com/10.1557/PROC-267-397.

[42] Haslach Jr HW. The moisture and rate-dependent mechanical properties of paper: A review. Mech Time-Dep Mater 2000;4(3):169–210. http://dx.doi.org/10.1023/A:1009833415827, URL http://link.springer.com/10.1023/A:1009833415827.

[43] Ko J, Cho K, Han SW, Sung HK, Baek SW, Koh W-G, et al. Hydrophilic surface modification of poly(methyl methacrylate)-based ocular prostheses using poly(ethylene glycol) grafting. Colloids Surfaces B 2017;158:287–94. http://dx.doi.org/10.1016/j.colsurfb.2017.07.017.

[44] Kanninen MF. An augmented double cantilever beam model for studying crack propagation and arrest. Int J Fract 1973;9:83–92. http://dx.doi.org/10.1007/BF00035958.

[45] Hutchinson JW, Evans AG. Mechanics of materials: Top-down approaches to fracture. Acta Mater 2000;48:125–35. http://dx.doi.org/10.1016/S1359-6454(99)00291-8.

[46] Gowrishankar S, Mei H, Liechti KM, Huang R. A comparison of direct and iterative methods for determining traction-separation relations. Int J Fract 2012;177:109–28. http://dx.doi.org/10.1007/s10704-012-9758-3.

[47] Rice J. A path independent integral and the approximate analysis of strain concentration by notches and cracks. J Appl Mech 1968;35:379–86.

[48] Rice JR. Mathematical analysis in the mechanics of fracture. In: Liebowitz H, editor. Fracture: An advanced treatise. New York: Academic Press; 1968, p. 191–311.

[49] Tvergaard V, Hutchinson JW. The relation between crack growth resistance and fracture process parameters in elastic-plastic solids. J Mech Phys Solids 1992;40(6):1377–97. http://dx.doi.org/10.1016/0022-5096(92)90020-3, URL https://www.sciencedirect.com/science/article/pii/0022509692900203.

[50] Kanninen MF, Popelar CH. Advanced fracture mechanics. New York: Oxford University Press; 1985.

[51] Thouless M, Yang Q. Chapter 7 - measurement and analysis of the fracture properties of adhesive joints. In: Dillard D, Pocius A, Chaudhury M, editors. Adhesion science and engineering. Amsterdam: Elsevier Science B.V.; 2002, p. 235–71. http://dx.doi.org/10.1016/B978-0-444-51140-9.50034-2.

[52] Caulfield D. Effect of moisture and temperature on the mechanical properties of paper. In: Perkins RW, Mark RE, Thorpe JL, editors. Solid mechanics advances in paper related industries. Proceedings of the national science foundation workshop, 1990, p. 50–62.

[53] Zauscher S, Caulfield DF, Nissan AH. The influence of water on the elastic modulus of paper. Tappi J 1997;80(1):214–23.

[54] River BH, Okkonen EA. Contoured wood double cantilever beam specimen for adhesive joint fracture tests. J Test Eval 1993;21(1):21–8. http://dx.doi.org/10.1520/JTE11737J.

[55] Long R, Hui C-Y. Fracture toughness of hydrogels: measurement and interpretation. Soft Matter 2016;12:8069–86. http://dx.doi.org/10.1039/C6SM01694D.

[56] Lee M, Kim S, Kim H-Y, Mahadevan L. Bending and buckling of wet paper. Phys Fluids 2016;28(4):042101. http://dx.doi.org/10.1063/1.4944659.

[57] Linvill E, Östlund S. The combined effects of moisture and temperature on the mechanical response of paper. Exp Mech 2014;54(8):1329–41. http://dx.doi.org/10.1007/s11340-014-9898-7.

[58] Chernysh IN, Spiewak R, Cambor CL, Purohit PK, Weisel JW. Structure, mechanical properties, and modeling of cyclically compressed pulmonary emboli. J Mech Behav Biomed Mater 2020;105:103699. http://dx.doi.org/10.1016/j.jmbbm.2020.103699.

[59] Liang X, Shin J, Magagnosc D, Jiang Y, Jin Park S, John Hart A, et al. Compression and recovery of carbon nanotube forests described as a phase transition. Int J Solids Struct 2017;122–123:196–209. http://dx.doi.org/10.1016/j.ijsolstr.2017.06.025.

[60] Liang X, Chernysh I, Purohit PK, Weisel JW. Phase transitions during compression and decompression of clots from platelet-poor plasma, platelet-rich plasma and whole blood. Acta Biomater 2017;60:275–90. http://dx.doi.org/10.1016/j.actbio.2017.07.011.

[61] Gibson LJ, Ashby MF. Cellular solids: Structure and properties. New York: Cambridge University Press; 1999.

[62] Negi V, Picu R. Mechanical behavior of cross-linked random fiber networks with inter-fiber adhesion. J Mech Phys Solids 2019;122:418–34. http://dx.doi.org/10.1016/j.jmps.2018.09.027, URL https://linkinghub.elsevier.com/retrieve/pii/S0022509618304824.

[63] Burke SR, Möbius ME, Hjelt T, Hutzler S. Properties of lightweight fibrous structures made by a novel foam forming technique. Cellulose 2019;26(4):2529–39. http://dx.doi.org/10.1007/s10570-018-2205-5, URL http://link.springer.com/10.1007/s10570-018-2205-5.